Electronic Supplementary Information for

Simultaneous photocatalytic H_2 generation and organic synthesis over crystalline-amorphous Pd nanocube decorated $Cs_3Bi_2Br_9$

Chunhua Wang,[a] Bo Weng,*[b] Yuhe Liao,[c] Biao Liu,[d] Masoumeh Keshavarz,[a] Yang Ding,[e] Haowei Huang,[b] Davy Verhaeghe,[b] Julian A. Steele,[b] Wenhui Feng,[f] Bao-Lian Su,[e] Johan Hofkens*[ag] and Maarten B. J. Roeffaers*[b]

[a]Department of Chemistry, KU Leuven, Celestijnenlaan 200F, 3001 Leuven, Belgium.
[b]cMACS, Department of Microbial and Molecular Systems, KU Leuven, Celestijnenlaan 200F, 3001 Leuven, Belgium.
[c]Guangzhou Institute of Energy Conversion, Chinese Academy of Sciences, Guangzhou 510640, P. R. China.
[d]Hunan Key Laboratory for Super-microstructure and Ultrafast Process, School of Physics and Electronics, Central South University, Changsha 410083, P. R. China.
[e]Laboratory of Inorganic Materials Chemistry (CMI), University of Namur, 61 rue de Bruxelles, B-5000, Namur, Belgium.
[f]Hunan Province Key Laboratory of Applied Environmental Photocatalysis, Changsha University, Changsha, 410022, P. R. China.
[g]Max Planck Institute for Polymer Research, Ackermannweg 10, 55128 Mainz, Germany.

*Corresponding authors
Email: maarten.roeffaers@kuleuven.be; johan.hofkens@kuleuven.be;
bo.weng@kuleuven.be

Table of Contents

1. Materials and reagents

Bismuth(III) bromide ($BiBr_3$, ≥98%), potassium palladium(II) chloride (K_2PdCl_4, 99%), potassium bromide (KBr, 99%), L-ascorbic acid (AA, 99%), poly(vinyl pyrrolidone) (PVP, M.W. z 55 000), benzyl alcohol (anhydrous, 99.8 %) were purchased from Sigma-Aldrich. Cesium bromide (CsBr, 99%) and benzotrifluoride (≥98%) were purchased from Alfa Aesar. Dimethyl sulfoxide (DMSO, anhydrous, Max. 0.005% water) was supplied by VWR chemicals. Ethanol (absolute, ≥99.8%) was purchased from Fisher Chemical. Bismuthiol I (1,3,4-thiadiazole-2,5-dithiol ($C_2H_2N_2S_3$), ≥99.0%) was purchased from Fluka. The Milli-Q water was obtained from the Milli-Q System. All chemicals were used without further purification.

2. Photocatalyst preparation

2.1 Preparation of $Cs_3Bi_2Br_9$ catalyst

$Cs_3Bi_2Br_9$ material was synthesized at room temperature using an anti-solvent precipitation method. Firstly, the $Cs_3Bi_2Br_9$ perovskite precursor solution was prepared by dissolving CsBr and $BiBr_3$ (CsBr/$BiBr_3$=3:2) in dimethyl sulfoxide (DMSO) at a precursor concentration of 0.4 M. Secondly, the fully dissolved $Cs_3Bi_2Br_9$ precursor solution was added to isopropanol to get the $Cs_3Bi_2Br_9$ suspension, and the $Cs_3Bi_2Br_9$ was collected by centrifugation. Finally, the suspension was dried in a vacuum oven at 60 ^oC overnight.

2.2 Synthesis of palladium nanocubes (Pd NCs)

The Pd NCs were synthesized according to the previously reported method.[1] First, PVP, KBr and AA with the amount of 105 mg, 600 mg, and 60 mg, respectively, were added in an 8 mL Milli-Q water, and under magnetic stirring at 80 ^oC for 10 min. Second, 3 mL Milli-Q water solution containing 63 mg K_2PdCl_4 was added to the above mixture under magnetic stirring at 80 ^oC for 3 h. Finally, the synthesized black Pd NCs were collected by centrifugation and washed with isopropanol, and then dispersed in isopropanol or methanol at a concentration of 1 mg/mL.

2.3 Synthesis of amorphous palladium (APd)

The APd was synthesized by a previously reported method with slight modification.[2]

In a typical experiment, 1 mL of the as-synthesized Pd NCs with a concentration of 1 mg/mL in methanol was mixed with 9 mL of a methanol solution containing 50 mg of bismuthiol I. The mixed solution was sealed in a closed vial under magnetic stirring at 25 ^{o}C for 8 h. After that, the APd products were collected by centrifugation and washed with isopropanol.

2.4 Synthesis of APd/$Cs_3Bi_2Br_9$ composite

A series of x wt% APd/$Cs_3Bi_2Br_9$ photocatalysts were synthesized at room temperature through the similar precipitation method mentioned above. In a typical experiment (1% APd/$Cs_3Bi_2Br_9$), 15 mL isopropanol containing 100 mg $Cs_3Bi_2Br_9$ powder was first kept stirring for 30 min, and then 20 mL of isopropanol solution containing 1 mg APd was added dropwise into the vigorously stirred $Cs_3Bi_2Br_9$ suspension. Then the mixture was kept stirring at room temperature for 12 h. Finally, the APd/$Cs_3Bi_2Br_9$ suspension was collected by centrifugation and dried in a vacuum oven at 60 ^{o}C.

3. Characterization

3.1 Instrumentations and methods

X-ray diffraction (XRD) patterns of the catalysts were achieved using an X-ray diffractometer (Cu Kα1 radiation, λ=1.5406 Å) in the 2 θ ranging from 10 to 70 degrees at a scan rate of 0.02^{o}/s. Scanning electron micrographs of samples were recorded by scanning electron microscopy (SEM, FEI-Q FEG250). Transmission electron microscopy (TEM) and high-resolution transmission electron microscopy (HRTEM) were analysed using a JEOL model JEM 2010 EX instrument at an acceleration voltage of 200 kV. Ultraviolet-visible spectrophotometer (UV-vis, Lambda-950) was employed to obtain the optical properties of the samples by UV-vis diffuse reflectance spectroscopy (DRS) in the wavelength of 300-800 nm, where $BaSO_4$ and black carbon were used as the references. Steady-state photoluminescence spectra were recorded on an Edinburgh FLS980 with an excitation wavelength of 365 nm in the wavelength of 425-575 nm. Time-resolved PL spectra were recorded on a Leica DMi8 system with a pulsed white light laser (SuperK Extreme EXW-12, NKT Photonics) operating at 405 nm and set at a repetition rate of 20

MHz and a fluence of 2 μJ mm^{-2}. X-ray photoelectron spectroscopy (XPS, Al Kα X-ray source, 1486.6 eV) was employed to study the chemical structure and valence state information of the materials, and the C 1s signal was set to a position of 284.6 eV. Photoelectrochemical measurements were carried out using a standard three-electrode setup. Ag/AgCl electrode was employed as the reference electrode, a platinum sheet was used as the counter electrode. The working electrode was deposited on a cleaned indium tin oxide (ITO) substrate and immersed in the electrolyte solution. Tetrabutylammonium hexafluorophosphate ($TBAPF_6$, 0.1 M) dissolved in dichloromethane (DCM) solution was used as the electrolyte. Electrochemical impedance spectroscopy (EIS) was obtained on an electrochemical workstation under an alternating current (AC) voltage (5 mV amplitude) in a frequency range from 10 kHz to 5 MHz with the open circuit potential of 0.2 V. Photocurrent response measurements were performed under simulated solar light irradiation. Cathodic polarization curves were achieved via linear sweep voltammetry technique with a scan rate of 0.2 mV/s. Mott−Schottky plots were measured in dark at a frequency of 1 kHz.

The surface charge transfer efficiency (η_t) was measured by adding methylviologen dichloride ($MVCl_2$) into the electrolyte as a fast electron scavenger.[3, 4] The photocurrent can be described by the following Equation.[4]

$$J_1 = J_m \times \eta_a \times \eta_s \times \eta_t \quad (1)$$

When adding $MVCl_2$ to the electrolyte, the surface charge transfer is very fast and the η_t approximately reaches 100%. The photocurrent can be written as Equation.[3]

$$J_2 = J_m \times \eta_a \times \eta_s \quad (2)$$

Due to J_m, η_a, η_s are unchanged before and after adding the $MVCl_2$, the surface transfer efficiency (η_t) can be given as:[3, 4]

$$\eta_t = J_1/J_2 \quad (3)$$

3.2 Density functional theory (DFT) calculation

The present calculations have been performed with the Vienna ab initio simulation package (VASP) code, based on density functional theory (DFT). Projector-augmented wave method is used to describe the interaction between ion cores and valence electrons. Atomic structures are optimized using the exchange-correlation functional of Perdew,

Burke, and Ernzerhof. A plane-wave cutoff of 400 eV is used in the calculation. Monkhorst-Pack 5×5×1 k-point grid is used to sample the Brillouin zone. All atoms are allowed to be fully relaxed till the atomic Hellmann-Feynman forces are less than 0.02 eV/Å. The convergence criterion of energy in the self-consistency process is set at about 1×10^{-4} eV. The plane-averaged charge density difference can be written as $\Delta\rho(z) = \rho_{\text{tot}} - \rho_{Cs_3Bi_2Br_9} - \rho_{APd.}$ Here, $\rho_{tot}$is the plane-averaged density of the combined APd/$Cs_3Bi_2Br_9$ system. $\rho_{Cs_3Bi_2Br_9}$ and ρ_{APd} are the plane-averaged densities of the free-standing $Cs_3Bi_2Br_9$ interface and APd interface, respectively, which are calculated by freezing the atomic positions of the respective components in the combined system.

3.3 Photocatalytic activity evaluation

The photocatalytic reactions were conducted in a 25 mL quartz reactor. In a typical experiment, 15 mg catalyst (1% APd/$Cs_3Bi_2Br_9$) and 1 mmol benzyl alcohol (BA) were added to 2.5 mL benzotrifluoride. Then, the mixture was evacuated by a mechanical pump to completely remove air, and under simulated solar light illumination (150 W Xe lamp) for 14 h. After the illumination, the amount of H_2 evolved was detected using a gas chromatograph (GC, Shimadzu 2014) equipped with a thermal conductivity detector (TCD). Then, the mixture was centrifuged, and the filtrates were analyzed by GC (Shimadzu 2010) to obtain the amount of the generated benzaldehyde (BAD). The conversion and selectivity of BA were defined as follows:

Conversion (%) = $[(C_0\text{-}C_A)/C_0] \times100\%$

Selectivity (%) = $[C_B/(C_0\text{-}C_A)] \times100\%$

Where C_0 is the initial concentration of BA, C_A and C_B are the concentrations of the BA substrate and corresponding BAD product, respectively.

The apparent quantum efficiency (AQE) for H_2 generation measured at 400 nm (light intensity: 9.02 mW/cm^2) is calculated according to the following equations:

AQE=(number of reacted electrons/number of incident electrons) ×100%

=(2×number of evolved H_2 electrons/number of incident electrons) ×100%

$=(2\times6.02\times10^{23}\times0.0025)/\{(14\times3600\times9.02)/[(6.6261\times10^{-34})\times(3\times10^{8})]/(4\times10^{-7})\}$

=0.33%

4. Main text supporting characterization

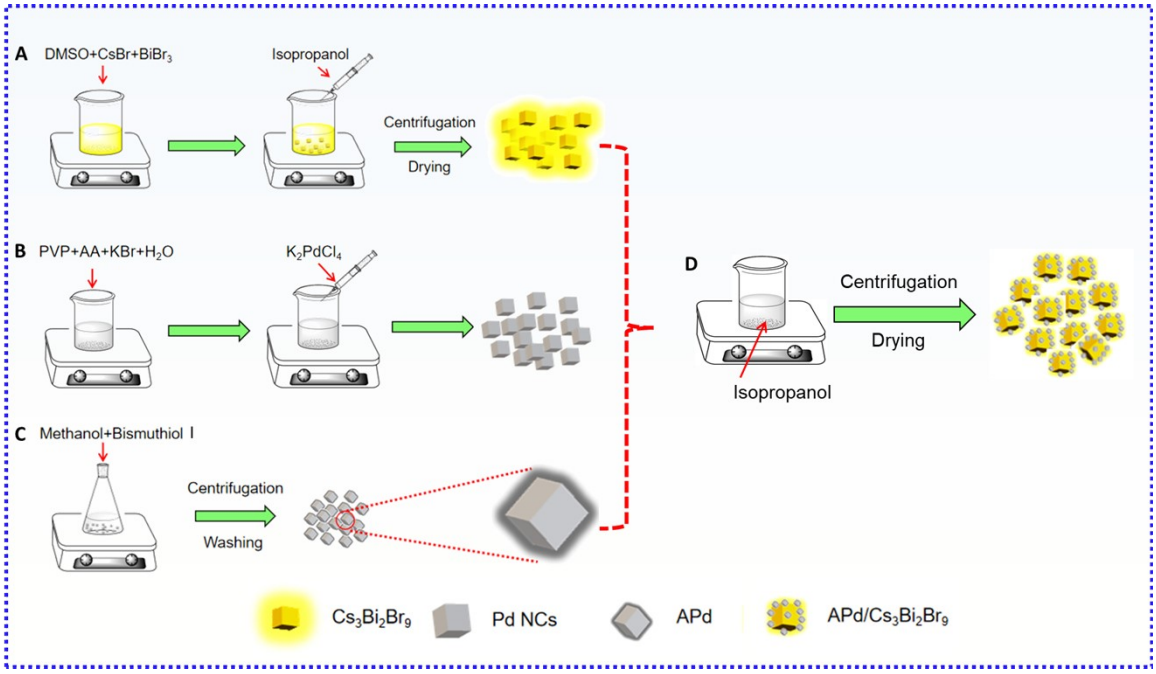

Fig. S1. The synthetic procedure of $Cs_3Bi_2Br_9$, Pd, APd, and APd/$Cs_3Bi_2Br_9$ materials.

Note: The $Cs_3Bi_2Br_9$ powder was synthesized by an antisolvent precipitation method using the $Cs_3Bi_2Br_9$ precursor solution with fully dissolved CsBr and $BiBr_3$ (CsBr/$BiBr_3$=3:2 in DMSO); Pd nanocubes (NCs) were synthesized according to the previous method,[1] and crystalline-amorphous Pd (APd) component was synthesized through modifying Pd NCs via a thiol molecule (bismuthiol I).[2] In the following, a series of APd/$Cs_3Bi_2Br_9$ hybrids with various Pd contents were synthesized by the decoration of the APd on the surface of $Cs_3Bi_2Br_9$ at room temperature, where the well-anchored APd NCs provide a crucial platform for charge transfer and interfacial redox reaction.

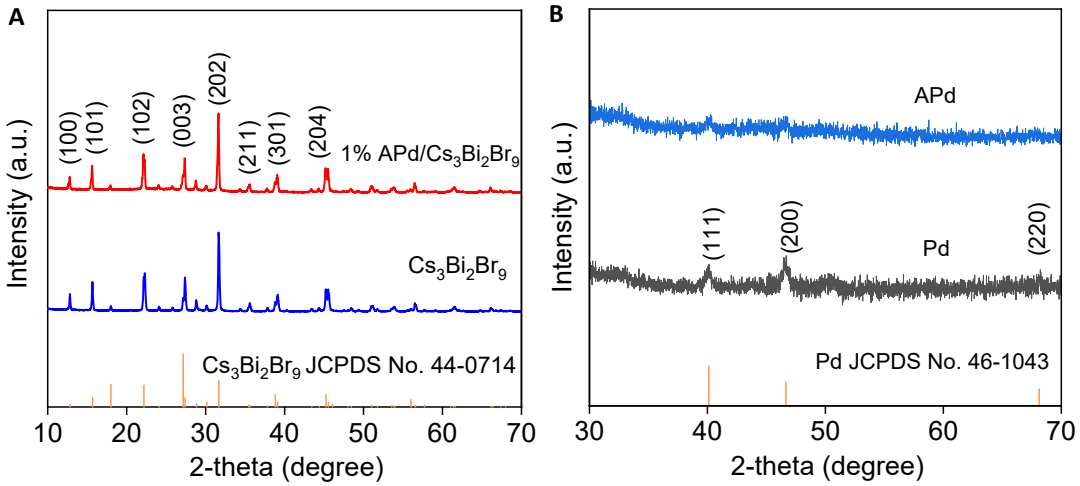

Fig. S2. XRD patterns of (A) $Cs_3Bi_2Br_9$ and 1% APd/$Cs_3Bi_2Br_9$ materials and (B) Pd and APd samples.

Note: This result reveals that the $Cs_3Bi_2Br_9$ in these hybrids is indexed to the trigonal phase (JCPDS No. 44-0714).[5] No typical diffraction peaks assigned to Pd in APd/$Cs_3Bi_2Br_9$ were detected due to the low content of APd (1%).[1] XRD patterns in Fig. S2B show the as-prepared crystalline Pd NCs possess obvious diffraction peaks, while the intensity of the peaks of APd decreased significantly, indicating the formation of crystalline-amorphous structure.[2] This can be attributed to the replacement of PVP by thiol molecules because thiol-metal bond is enthalpically more favourable than pyrrolidone oxygen/nitrogen metal coordination.[6] Meanwhile, the attached hydrophilic or amphiphilic thiol ligands will be dissolved in an alcohol solution to some extent, which leads to the displacement of Pd, thus forming this crystalline-amorphous structure.[7]

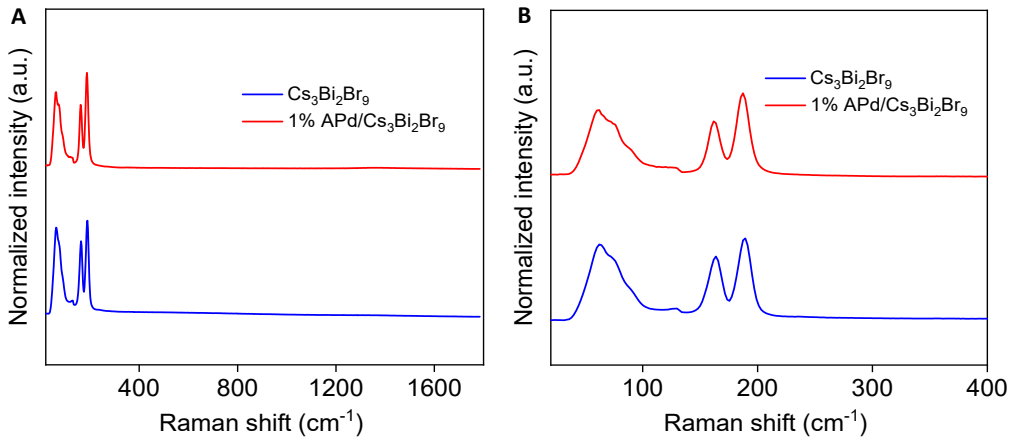

Fig. S3. Raman spectra of $Cs_3Bi_2Br_9$ and 1% APd/$Cs_3Bi_2Br_9$ materials in the range of (A) 20-1800 cm^{-1} and (B) 20-400 cm^{-1}.

Note: Raman spectroscopy further confirmed that $Cs_3Bi_2Br_9$ is the predominant species and APd deposition does not affect the structure of $Cs_3Bi_2Br_9$. The modes at 167 and 192 cm^{-1} are attributed to the stretching vibrations of Bi−Br bonds in $BiBr_6$ octahedra.[8] The other two peaks located at 63.9 and 74.6 cm^{-1} are due to vibrations of Br atoms only.[8, 9] The two samples decorated with APd correspond to the $Cs_3Bi_2Br_9$ vibrational mode, suggesting that $Cs_3Bi_2Br_9$ are the predominant species, agreeing with the XRD results.

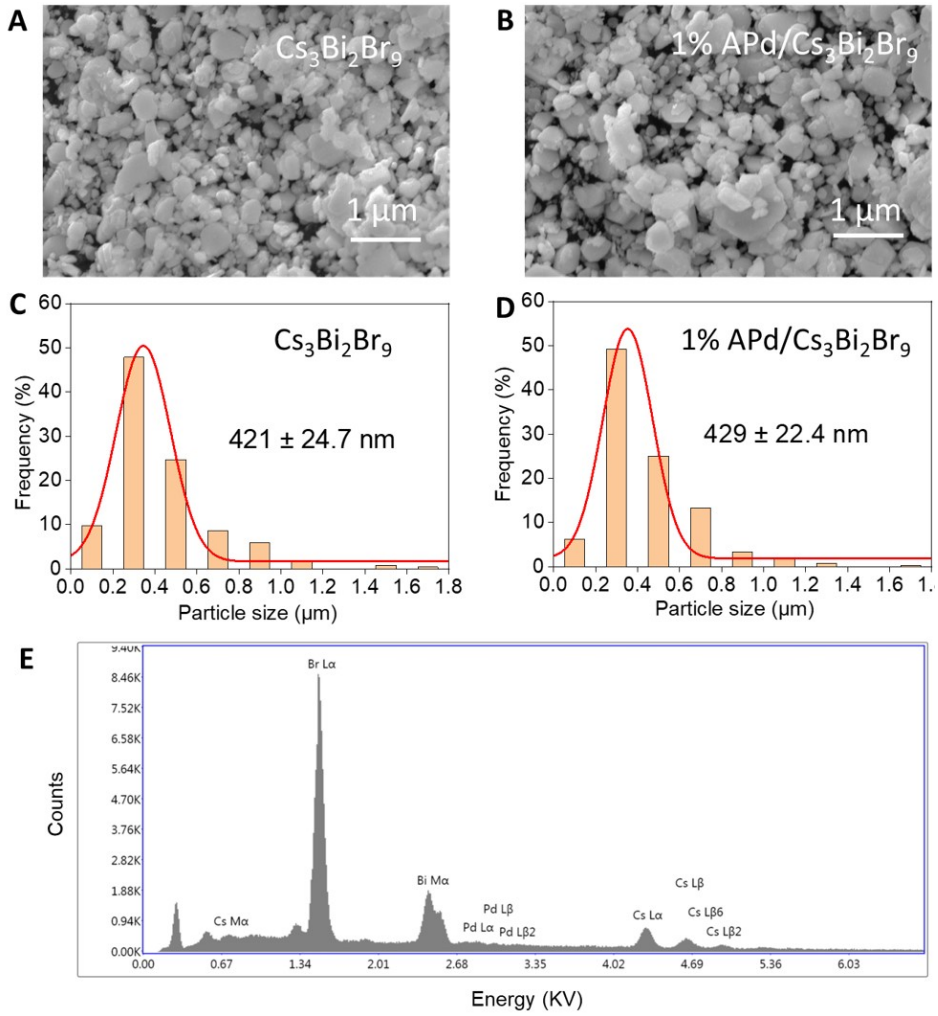

Fig. S4. (A-B) SEM images of (A) $Cs_3Bi_2Br_9$ and (B) 1% APd/$Cs_3Bi_2Br_9$ materials. (C-D) Particle size distribution of (C) $Cs_3Bi_2Br_9$ and (D) 1% APd/$Cs_3Bi_2Br_9$. (E) EDS spectra recorded for 1% APd/$Cs_3Bi_2Br_9$.

Note: The surface morphology of materials recorded through the scanning electron microscope (SEM) reveals the average size of $Cs_3Bi_2Br_9$ is around 520 nm; after loading APd, the resultant samples show a similar morphology relative to the blank $Cs_3Bi_2Br_9$. Energy-dispersive X-ray spectroscopy (EDS) spectrum confirmed the Cs, Bi, Br and Pd elements in the hybrid materials.

Table S1. The inductively coupled plasma-mass spectrometry (ICP-MS) result of Pd content in 1% APd/$Cs_3Bi_2Br_9$ sample.

Sample	Theoretical value (Pd content)	ICP-MS (Pd content)
1% APd/$Cs_3Bi_2Br_9$	1%	0.96%

Note: Inductively coupled plasma-mass spectrometry (ICP-MS) confirmed the amount of Pd in 1% APd/$Cs_3Bi_2Br_9$ sample is 0.96 wt%, which matches the theoretical value.

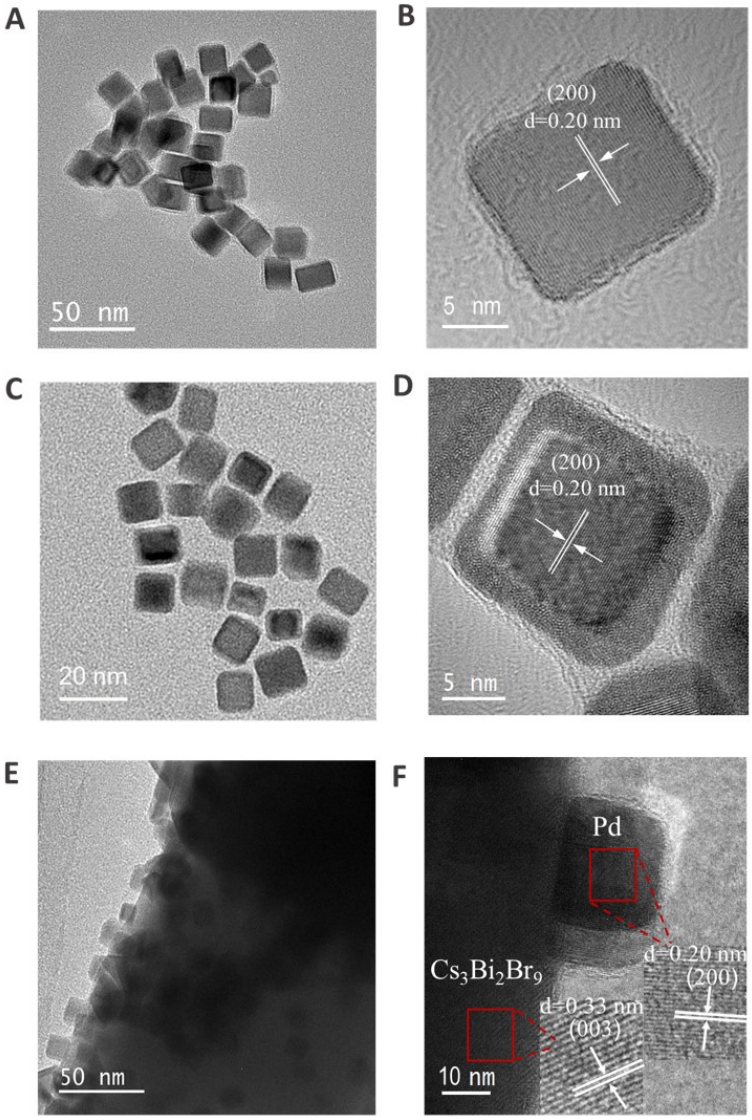

Fig. S5. Transmission electron microscopy (TEM) and high-resolution TEM (HRTEM) images of (A and B) Pd NCs, (C and D) APd NCs and (E and F) 1% APd/$Cs_3Bi_2Br_9$ material, respectively.

Note: TEM confirms the synthesized Pd has a cube morphology (Fig. S5A), HRTEM image shows that the lattice fringe of 0.20 nm corresponds to Pd (200)[1] crystal facet (Fig. S5B). The amorphization of the surface of APd leading to a crystalline-amorphous core@shell structure (Fig. S5D), and the lattice fringes of 0.33 nm and 0.20 nm in 1% APd/$Cs_3Bi_2Br_9$ (Fig. S5F) corresponding to $Cs_3Bi_2Br_9$ (003)[5] and Pd (200),[1] respectively.

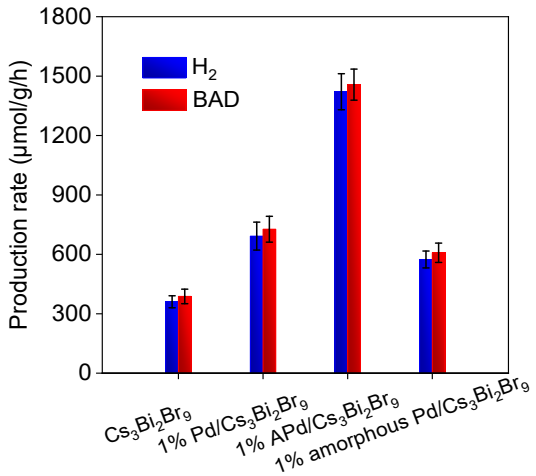

Fig. S6. Comparison of the photocatalytic performance of pure $Cs_3Bi_2Br_9$, and $Cs_3Bi_2Br_9$ coupled with crystalline Pd (1% Pd/$Cs_3Bi_2Br_9$), crystalline-amorphous Pd (1% APd/$Cs_3Bi_2Br_9$) and fully amorphous Pd (1% amorphous Pd/$Cs_3Bi_2Br_9$) composites. Reaction conditions: 1 mmol BA, 15 mg catalyst, 2.5 mL benzotrifluoride, simulated solar light (AM 1.5G, 150 W Xe lamp, light intensity: 100 mW/cm^2), reaction time (14 h).

Note: This result shows that the photoactivity of photocatalysts with crystalline-amorphous Pd cocatalyst is superior to that of pure crystalline and fully amorphous Pd, confirming the beneficial effect of partially surface amorphization of Pd.

Table S2. Comparison of photocatalytic H_2 evolution over various MHP-based photocatalysts.

Photocatalyst	Light source	Medium	H_2 production rate ($\mu mol\ g^{-1}\ h^{-1}$)	Ref.
$Cs_3Bi_2Br_9$/APd	AM 1.5G, 150 W	BA/BTF	1421	This Work
$MAPbBr_3$	$\lambda \geq 420$ nm	HI/HBr acid mix solution	11.20	[10]
$MAPbBr_3$	$\lambda \geq 420$ nm	HI acid	11.31	[11]
$MAPbBr_3$	$\lambda \geq 420$ nm, 300 W Xe	HI solution	14.00	[12]
DMF-$MAPbBr_3$	$\lambda \geq 420$ nm	HI acid	22.62	[11]
DMSO-$MAPbBr_3$	$\lambda \geq 420$ nm	HI acid	31.67	[11]
$MAPbI_3$	$\lambda \geq 475$ nm	HI solution	33	[11]
$MAPbBr_3$/Pt	$\lambda \geq 420$ nm	HI/HBr solution	33.60	[10]
$MAPbBr_3$	$\lambda \geq 420$ nm	Saturated HI solution	38.00	[13]
$MAPbBr_3$/Pt	$\lambda \geq 420$ nm, 300 W Xe	HI solution	40.00	[12]
$CsAgBiBr_4$/rGO	$\lambda \geq 420$ nm, 300 W Xe	HBr acid	50	[14]
$MAPbBr_3$/Pt	$\lambda \geq 420$ nm	Saturated HI solution	90	[13]
$CsPbBr_3$/Ru@TiO_2	445 nm, 50 mW laser	Triethanolamine	160	[15]
$MA_3Bi_2I_9$/Pt	$\lambda \geq 400$ nm, 300 W	HI solution	170	[16]
$MAPbI_3$/TiO_2	AM 1.5G	HI acid	436.6	[13]
PEDOT:PSS/$MAPbBr_3$/Ta_2O_5	$\lambda \geq 420$ nm), 150 mW/cm^2	HBr solution	650	[17]
$DMASnBr_3$/g-C_3N_4	500 W cm^{-2} Xe	Glucose solution	925	[18]

$MAPbBr_{3-x}I_x$/Pt	λ ≥ 420 nm), 300 W	HBr/HI solution	2604.80	[10]
BP/$MAPbI_3$	λ ≥ 420 nm), 300 mW/cm^2	HI solution	3742	[19]

BA: benzyl alcohol. BTF: benzotrifluoride

Table S3. Comparison of selective photocatalytic oxidation of benzyl alcohol (BA) to benzaldehyde (BAD) over various MHP-based photocatalysts.

Photocatalyst	Light source	Medium	BAD production rate (μmol g^{-1} h^{-1})	Ref.
$Cs_3Bi_2Br_9$/APd	AM 1.5G, 150 W	BA/BTF	1457	This work
$FAPbBr_3$	AM1.5 G	Trifluorotoluene	18	[20]
$FAPbBr_3/Bi_2WO_6$	AM 1.5G	Trifluorotoluene	250	[20]
$CsPbBr_3/TiO_2$	λ >420 nm, 300W	Toluene	500	[21]
$FAPbBr_3/Bi_2WO_6$	AM1.5 G, 150W	Trifluorotoluene	580	[20]
$FAPbBr_3/TiO_2$	AM1.5G, 150W	Toluene	800	[22]
$CsPbX_3/W_{18}O_{49}$	AM1.5G, 150W	Hexane	1000	[23]
$Cs_3Bi_2Br_9/TiO_2$	λ >420 nm, 300W	Toluene	1465	[24]

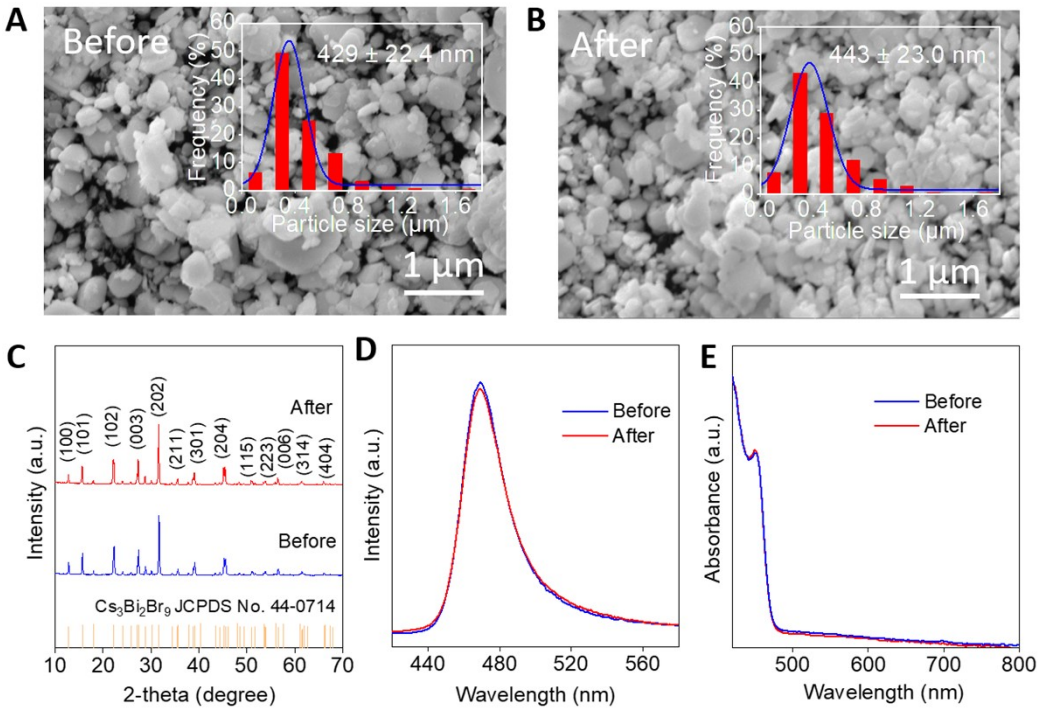

Fig. S7. (A-B) SEM images of 1% APd/$Cs_3Bi_2Br_9$ material (A) before and after five reaction cycles. (C) XRD, (D) PL and (E) Absorption spectra of 1% APd/$Cs_3Bi_2Br_9$ before and after recycling measurements, respectively.

Note: This result shows that there are negligible changes in morphology, structure and optical properties of the material after the recycling test.

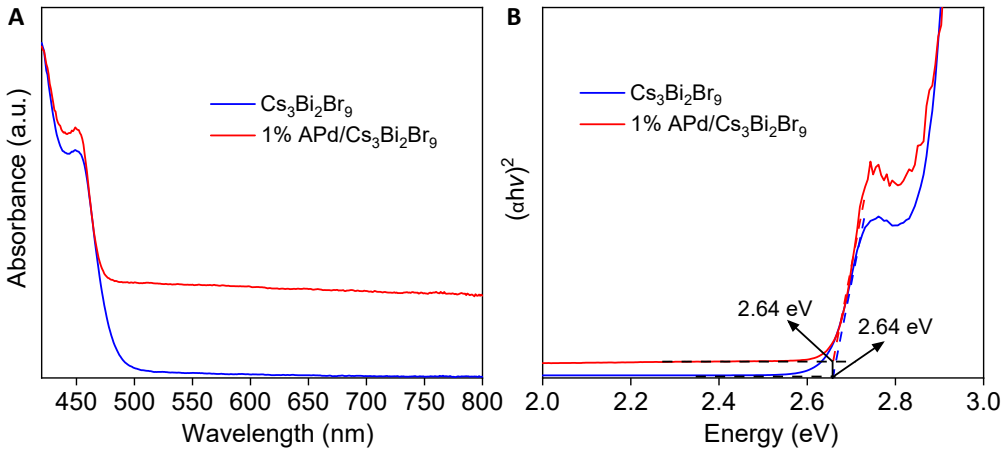

Fig. S8. (A) DRS spectra and (B) Tauc plots of $Cs_3Bi_2Br_9$ and 1% APd/$Cs_3Bi_2Br_9$ materials.

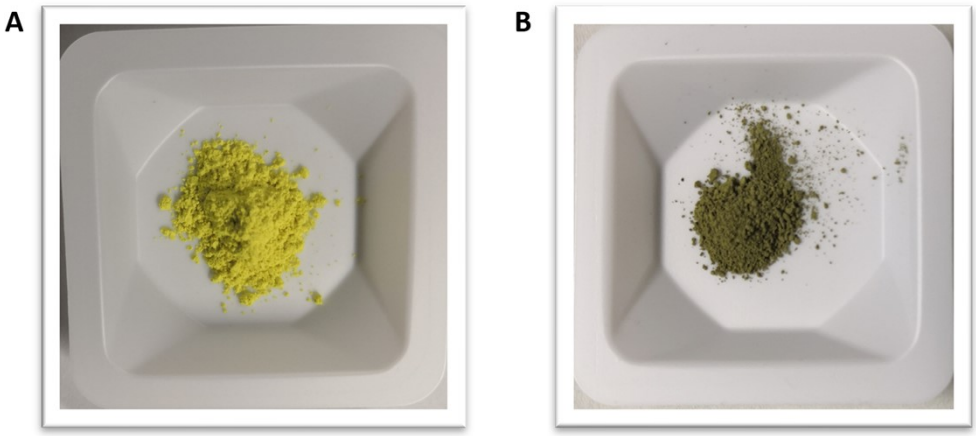

Fig. S9. The digital photographs of (A) $Cs_3Bi_2Br_9$ and (B) 1% APd/$Cs_3Bi_2Br_9$ materials.

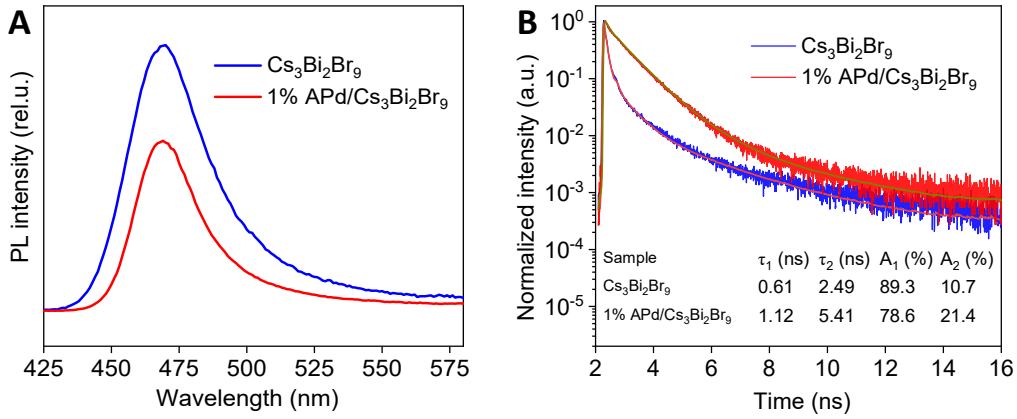

Fig. S10. (A) Steady-state PL spectra and (B) time-resolved PL decays of $Cs_3Bi_2Br_9$ and 1% APd/$Cs_3Bi_2Br_9$ materials.

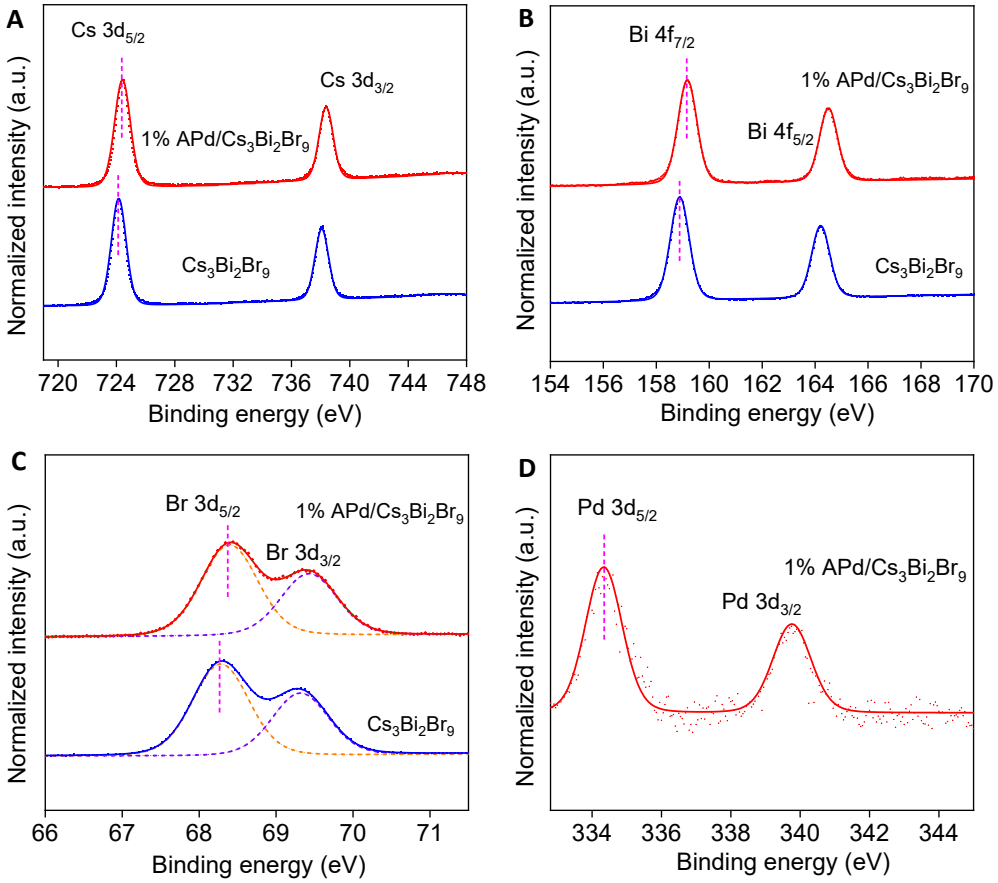

Fig. S11. High-resolution XPS spectra of (A) Cs 3d, (B) Bi 4f, (C) Br 3d core levels of $Cs_3Bi_2Br_9$ and 1% APd/$Cs_3Bi_2Br_9$ and (D) Pd 3d core level of 1% APd/$Cs_3Bi_2Br_9$.

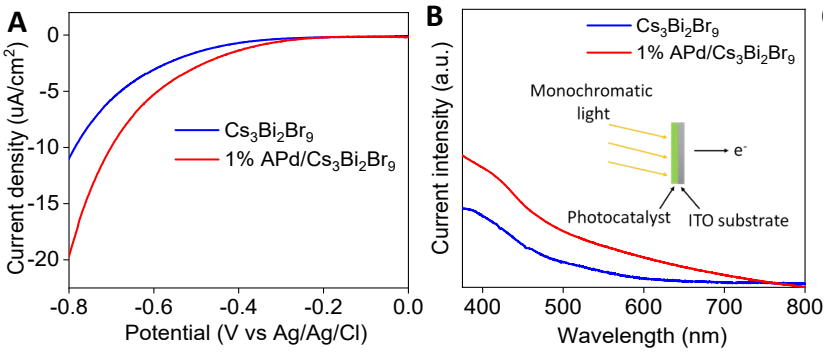

Fig. S12. (A) Polarization curves and (B) Photocurrent response versus monochromatic light under the potential of 0.06 V of $Cs_3Bi_2Br_9$ and 1% APd/$Cs_3Bi_2Br_9$ materials.

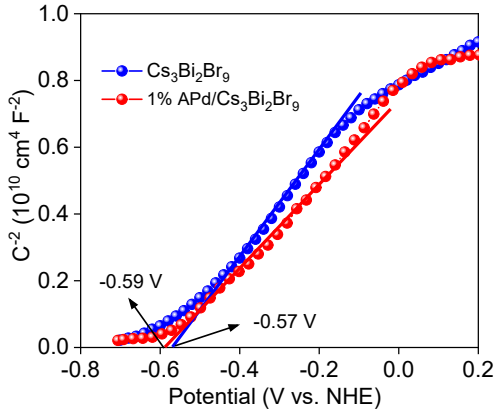

Fig. S13. Mott-Schottky plots of $Cs_3Bi_2Br_9$ and 1% APd/$Cs_3Bi_2Br_9$ measured in dark at the frequency of 1 kHz.

Note: Based on the slopes of the Mott-Schottky plots, the flat band potentials of $Cs_3Bi_2Br_9$ and 1% APd/$Cs_3Bi_2Br_9$ are concluded to be -0.57 V and -0.59 V, respectively, and the density of the charge carrier (N_D) of pure $Cs_3Bi_2Br_9$ and 1% APd/$Cs_3Bi_2Br_9$ can be calculated according to the following equation:[25-27]

$$N_D = \frac{2}{q\varepsilon\varepsilon_0}\frac{dE}{d\frac{1}{C^2}} = \frac{2}{q\varepsilon\varepsilon_0}\frac{1}{slope}$$

where N_D is the density of charge carriers, C is the space charge capacitance, E denotes the

applied potential, q is the electric charge (1.602×10^{-19} C), ε and ε_0 refer to the dielectric constant of the semiconductor (13.8)[28] and permittivity in a vacuum (8.85×10^{-12} F m^{-1}). The calculated N_D of 1% APd/$Cs_3Bi_2Br_9$ is 8.28×10^{19} cm^{-3}, slightly larger than that of pure $Cs_3Bi_2Br_9$ (6.43×10^{19} cm^{-3}), showing that an enhanced carrier densities after the decoration of APd NCs.

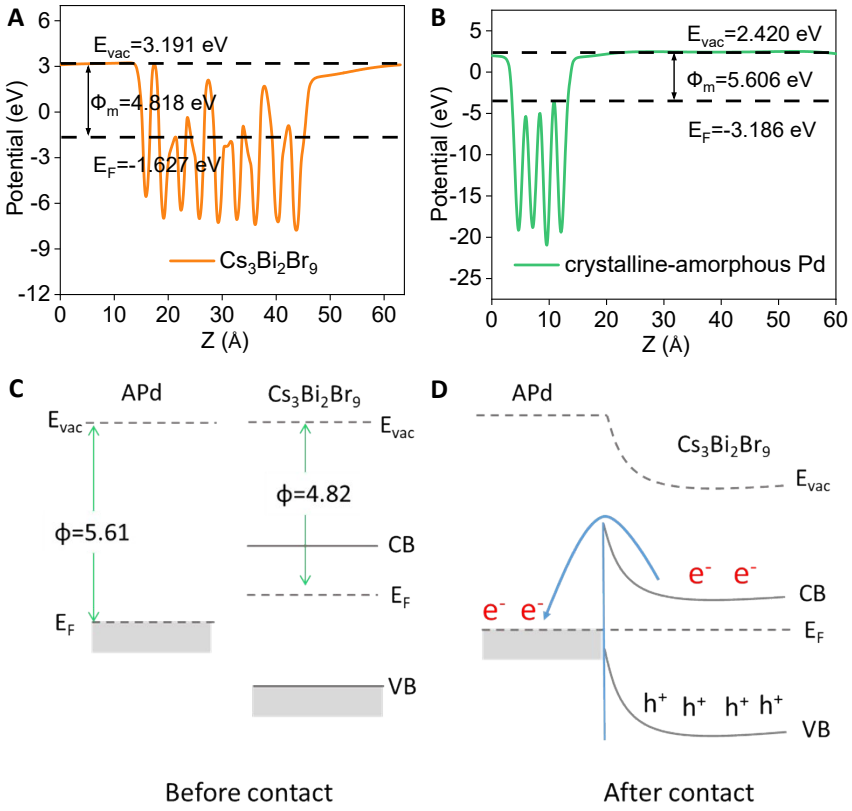

Fig. S14. The work function of (A) $Cs_3Bi_2Br_9$ and (B) APd materials. (C) Schematic energy diagram of APd and $Cs_3Bi_2Br_9$. (D) Schematic band diagram of APd/$Cs_3Bi_2Br_9$ composites illustrating the charge transfer driven by a Schottky junction, where E_{vac}, E_F, CB, and VB represent vacuum level, Fermi level, conduction band and valence band, respectively.

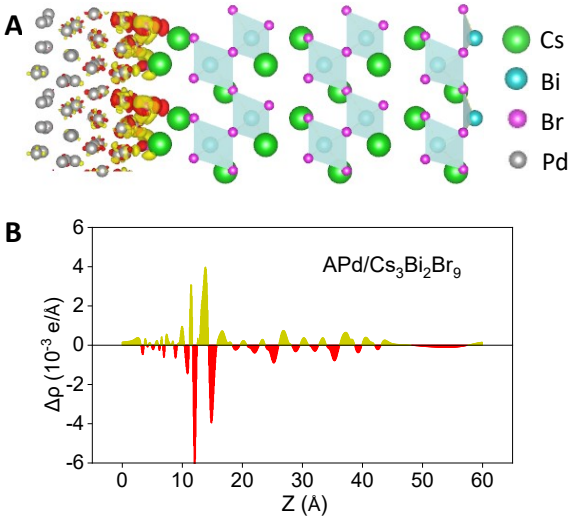

Fig. S15. (A) Charge density difference and (B) planar-averaged differential charge density of APd/$Cs_3Bi_2Br_9$ interface. The yellow and red areas represent electron accumulation and depletion, respectively.

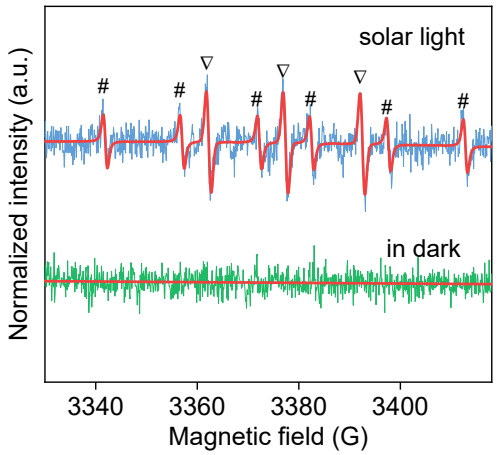

Fig. S16. ESR spectra of DMPO-carbon centered radical (#) and nitroxide-like radical (▽) over APd/$Cs_3Bi_2Br_9$ samples in BA and benzotrifluoride mixture.

Note: This result indicates the generation of $C_6H_5CH(OH)^{\bullet}$* free radicals during the photocatalytic reaction process. Namely, photocatalytic selective BA oxidation occurs via carbon-centered radicals.

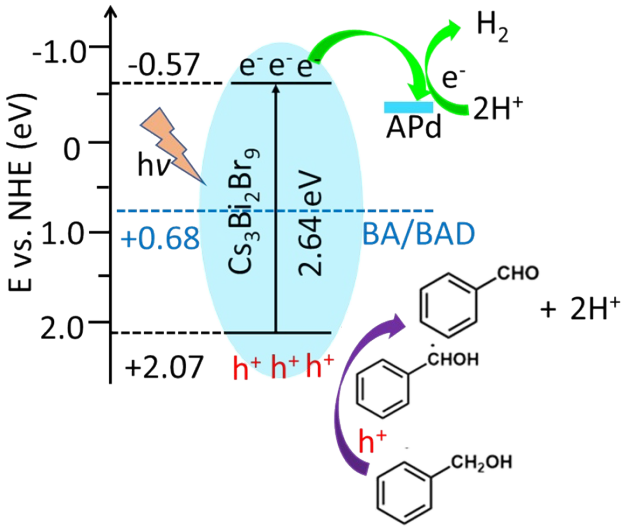

Fig. S17. Proposed reaction mechanism for the dual-functional photocatalytic system for dehydrogenation of BA with simultaneous H_2 and BAD production over APd/$Cs_3Bi_2Br_9$ photocatalyst.

5. References

1. B. Weng, Q. Quan and Y.-J. Xu, *J. Mater. Chem. A*, 2016, **4**, 18366-18377.
2. H. Cheng, N. Yang, G. Liu, Y. Ge, J. Huang, Q. Yun, Y. Du, C. J. Sun, B. Chen, J. Liu and H. Zhang, *Adv. Mater.*, 2020, **32**, e1902964.
3. C. Feng, L. Tang, Y. Deng, J. Wang, Y. Liu, X. Ouyang, H. Yang, J. Yu and J. Wang, *Appl. Catal. B: Environ.*, 2021, **281**, 119539.
4. C. Feng, L. Tang, Y. Deng, J. Wang, J. Luo, Y. Liu, X. Ouyang, H. Yang, J. Yu and J. Wang, *Adv. Funct. Mater.*, 2020, **30**, 2001922.
5. B. Yang, J. Chen, F. Hong, X. Mao, K. Zheng, S. Yang, Y. Li, T. Pullerits, W. Deng and K. Han, *Angew. Chem. Int. Ed.*, 2017, **56**, 12471-12475.
6. S. Zhang, S. Kim and V. V. Tsukruk, *Langmuir*, 2017, **33**, 3576-3587.
7. C. Vericat, M. E. Vela, G. Benitez, P. Carro and R. C. Salvarezza, *Chem.. Soc Rev.*, 2010, **39**, 1805-1834.
8. G. Bator, J. Baran, R. Jakubas and M. Karbowiak, *Vib. Spectr.*, 1998, **16**, 11-20.
9. M. Y. Valakh, M. Lisitsa, E. Y. Peresh, O. Trylis and A. Yaremko, *J. Mol. Struct.* 1997, **436**, 309-313.
10. Y. Wu, P. Wang, Z. Guan, J. Liu, Z. Wang, Z. Zheng, S. Jin, Y. Dai, M.-H. Whangbo and B. Huang, *ACS Catal.*, 2018, **8**, 10349-10357.
11. S. Park, W. J. Chang, C. W. Lee, S. Park, H.-Y. Ahn and K. T. Nam, *Nat. Energy*, 2016, **2**, 1-6.
12. Y. Wu, P. Wang, X. Zhu, Q. Zhang, Z. Wang, Y. Liu, G. Zou, Y. Dai, M. H. Whangbo and B. Huang, *Adv. Mater.*, 2018, **30**, 1704342.
13. X. Wang, H. Wang, H. Zhang, W. Yu, X. Wang, Y. Zhao, X. Zong and C. Li, *ACS Energy Lett.*, 2018, **3**, 1159-1164.
14. T. Wang, D. Yue, X. Li and Y. Zhao, *Appl. Catal. B: Environ.*, 2020, **268**, 118399.
15. M. V. Pavliuk, M. Abdellah and J. Sá, *Mater. Today Commun.*, 2018, **16**, 90-96.
16. Y. Guo, G. Liu, Z. Li, Y. Lou, J. Chen and Y. Zhao, *ACS Sustain. Chem. Eng.*, 2019, **7**, 15080-15085.
17. H. Wang, X. Wang, R. Chen, H. Zhang, X. Wang, J. Wang, J. Zhang, L. Mu, K. Wu and F. Fan, *ACS Energy Lett.*, 2018, **4**, 40-47.
18. A. Speltini, L. Romani, D. Dondi, L. Malavasi and A. Profumo, *Catalysts*, 2020, **10**,

1259.

19. R. Li, X. Li, J. Wu, X. Lv, Y.-Z. Zheng, Z. Zhao, X. Ding, X. Tao and J.-F. Chen, *Appl. Catal. B: Environ.*, 2019, **259**, 118075.
20. H. Huang, J. Zhao, Y. Du, C. Zhou, M. Zhang, Z. Wang, Y. Weng, J. Long, J. Hofkens and J. A. Steele, *ACS Nano*, 2020, **14**, 16689-16697.
21. S. Schunemann, M. van Gastel and H. Tuysuz, *ChemSusChem*, 2018, **11**, 2057-2061.
22. H. Huang, H. Yuan, K. P. F. Janssen, G. Solís-Fernández, Y. Wang, C. Y. X. Tan, D. Jonckheere, E. Debroye, J. Long, J. Hendrix, J. Hofkens, J. A. Steele and M. B. J. Roeffaers, *ACS Energy Lett.*, 2018, **3**, 755-759.
23. R. Cheng, J. A. Steele, M. B. Roeffaers, J. Hofkens and E. Debroye, *ACS Appl. Energy Mater.*, 2021, **4**, 3460-3468.
24. Q. Sun, W. Ye, J. Wei, L. Li, J. Wang, J.-H. He and J.-M. Lu, *J. Alloys Compd*, 2022, **893**, 162326.
25. I. A. Digdaya, L. Han, T. W. Buijs, M. Zeman, B. Dam, A. H. Smets and W. A. Smith, *Energy Environ. Sci.*, 2015, **8**, 1585-1593.
26. Q. Wang, S. Yu, W. Qin and X. Wu, *Nanoscale Adv.*, 2020, **2**, 274-285.
27. H. Zhang, L. Ma, J. Ming, B. Liu, Y. Zhao, Y. Hou, Z. Ding, C. Xu, Z. Zhang and J. Long, *Appl. Catal. B: Environ.*, 2019, **243**, 481-489.
28. X. Li, P. Zhang, Y. Hua, F. Cui, X. Sun, L. Liu, Y. Bi, Z. Yue, G. Zhang and X. Tao, *ACS Appl. Mater. Interfaces*, 2022, **14**, 9340-9351.